RESEARCH ARTICLE | SEPTEMBER 08 2025

Same-group element replacement enhances superconductivity in clathrate-like YH_4

Xuejie Li; Yuzhou Hao; Yujie Liu; Xiaoying Wang; Turab Lookman ; Jun Sun; Xiangdong Ding ; Zhibin Gao

J. Chem. Phys. 163, 104107 (2025)
https://doi.org/10.1063/5.0271662

The Journal of Chemical Physics ARTICLE pubs.aip.org/aip/jcp

Same-group element replacement enhances superconductivity in clathrate-like YH_4

Cite as: J. Chem. Phys. 163, 104107 (2025); doi: 10.1063/5.0271662
Submitted: 19 March 2025 • Accepted: 19 August 2025 •
Published Online: 8 September 2025

Xuejie Li,[1] Yuzhou Hao,[1] Yujie Liu,[1] Xiaoying Wang,[1] Turab Lookman,[1,2] Jun Sun,[1] Xiangdong Ding,[1] and Zhibin Gao[1,a)]

AFFILIATIONS

[1] State Key Laboratory for Mechanical Behavior of Materials, School of Materials Science and Engineering, Xi'an Jiaotong University, Xi'an 710049, China

[2] AiMaterials Research LLC, Santa Fe, New Mexico 87501, USA

[a)] **Author to whom correspondence should be addressed:** zhibin.gao@xjtu.edu.cn

ABSTRACT

H_3S, LaH_{10}, and hydrogen-based compounds have garnered significant interest due to their high-temperature superconducting properties. However, the requirement for extremely high pressures limits their practical applications. In this study, YH_4 is adopted as a base material, with partial substitution of yttrium (Y) by scandium (Sc), lanthanum (La), and zirconium (Zr). Pure YH_4, stable at 120 GPa, exhibits a critical temperature (T_c) of 84–95 K. Substituting half of the Y atoms increases T_c to 124.43 K for (Y,Sc)H_4 at 100 GPa but reduces it to 101.24 K for (Y,La)H_4 at 120 GPa. In contrast, (Y,Zr)H_4 at 200 GPa shows a further suppressed T_c of 69.55 K. The remarkable superconductivity in (Y,Sc)H_4 might be related to its unique phonon dispersion without an optical-acoustic gap, compressed Y–H bonds, and significant electron delocalization under pressure, collectively boosting electron–phonon interactions. Furthermore, the lowest optical phonons play a crucial role in the superconductivity of these materials. This work suggests that substituting Y with same-group metal elements is an effective strategy to enhance T_c in hydride superconductors.

I. INTRODUCTION

Superconducting materials have drawn significant attention and are pivotal to the next industrial revolution. Among these, hydrogen-rich compounds (H-series compounds) have emerged as a prominent focus in superconductivity research due to their exceptionally high critical transition temperatures (T_c), approaching ambient conditions.[1–3] Notably, research conducted between 2014 and 2015 revealed that H_3S exhibited an exceptionally high critical temperature T_c of 203 K at around 90 GPa, as confirmed by both experimental and theoretical studies.[4,5] A major breakthrough came in 2019 when experiments verified that LaH_{10} in the $Fm\bar{3}m$ structure exhibits superconductivity at 170 GPa, reaching a T_c of ~250 K. These breakthroughs have spurred extensive research, significantly expanding the family of hydrogen-based superconductors through both experimental studies[6–15] and theoretical predictions.[16–25]

In recent years, numerous hydrogen-containing superconducting materials featuring yttrium (Y) as a key element have been discovered, demonstrating remarkable superconducting properties. For instance, YH_9 with a $P6/mmm$ symmetry at 201 GPa exhibits a T_c of 243 K,[11] while YH_6 in the $Im\bar{3}m$ symmetry at 166 GPa achieves a T_c of 224 K in the experimental research.[12] Among materials with even higher T_c values in theoretical research, the sodalite-like FCC YH_{10} stands out, reaching 305–326 K at 250 GPa.[26] Beyond these binary hydrides, ternary hydrides incorporating Y have also shown exceptional superconducting characteristics. For example, in theoretical research, the cubic $Fd\bar{3}m$ structure of $CaYH_{12}$, stable at 170 GPa, demonstrates a T_c of 258 K at 200 GPa.[27] Similarly, $Pm\bar{3}m$-$YCaH_{12}$ is estimated to have a T_c of 230 K at 180 GPa and remains stable at 200 GPa.[28]

Despite the promising superconducting properties of the aforementioned binary and ternary hydrides, their reliance on extraordinarily high pressures severely limits practical applications. The primary challenge in developing hydrogen-based superconductors is achieving high T_c at reduced pressures, which has prompted exploration of multiple approaches. For example, in theoretical research, the T_c of α-MoB_2, initially 37 K at 90 GPa, can be increased to ~43 K through electron doping.[29] Similarly, two-dimensional hydrogenated MgB_2 achieves a T_c exceeding 100 K under biaxial tensile strain in theoretical predictions.[30] In addition, HCP-(La,Ce)H_{9-10},

synthesized experimentally at 100 GPa, exhibits a high T_c of 176 K, demonstrating its potential for high-temperature superconductivity.[31] Nevertheless, several limitations remain: the prohibitive cost of using rare-earth elements (La, Ce) as dopants at the same time, the inherently low T_c of α-MoB_2, and the implementation difficulties associated with two-dimensional hydrogenation of MgB_2.

Building on the aforementioned discussion, we utilize YH_4 as the base material and create new compounds by substituting half of the Y atoms with Sc, La, and Zr, respectively. In this study, we determine the stabilization pressures for these three materials and employ calculations of differential charge density, Fermi surfaces, electronic band structures, and density of states to elucidate their electronic properties. In addition, we investigate their phonon characteristics, including phonon dispersion and phonon density-of-state distribution. The T_c ranges are determined using two distinct methods, with the effective Coulomb pseudopotential parameter (μ^*) set to 0.05 and 0.4. Among the materials studied, (Y,Sc)H_4 at 100 GPa exhibits the highest T_c and requires a lower synthesis pressure compared to the base material YH_4. Our findings demonstrate that substituting Y with same-group metal elements effectively enhances T_c, while substituting with neighboring elements significantly reduces the superconducting performance of the material.

II. COMPUTATIONAL METHODS

The lattice constants of the calculated materials were optimized using the Vienna *ab initio* Simulation Package (VASP),[32,33] employing the Perdew–Burke–Ernzerhof (PBE)[34] Generalized Gradient Approximation (GGA).[35,36] This optimization facilitated the calculation and analysis of electronic properties, including density of states, electronic band structures, and differential charge density, as well as phonon properties, such as the phonon spectrum and phonon density of states. For both self-consistent and non-self-consistent electron computations, a k-point grid of $12 \times 12 \times 6$ was used, with an energy cutoff of 350 eV. Structural optimization was considered complete when the maximum energy and force converged to below 10^{-6} eV/Å and 1 meV/Å, respectively.

The electron–phonon coupling (EPC), spectral function, and superconducting properties were computed using the Quantum-ESPRESSO (QE)[37] package with optimized norm-conserving Vanderbilt (ONCV)[38] pseudopotentials and the density functional perturbation theory (DFPT) method. Calculations utilized a charge density cutoff of 1040 Ry, a kinetic energy cutoff of 130 Ry, and k-point and q-point grids of $12 \times 12 \times 6$ and $6 \times 6 \times 3$, respectively. The isotropic Migdal–Eliashberg equations were solved using the EPW program[39,40] and the ELK code.[2,41,42]

With the effective Coulomb pseudopotential parameters μ^* ranging from 0.05 to 0.40, the McMillan–Allen–Dynes formula[43] is utilized to calculate the T_c of (Y,Sc,Zr,La)H_4,

$$T_c = \frac{\omega_{\log}}{1.2} \exp\left[-\frac{1.04(1+\lambda)}{\lambda - \mu^*(1+0.62\lambda)}\right]. \tag{1}$$

The electron–phonon coupling constant integrated over an integrated domain is

$$\lambda(\omega) = 2\int_0^{\omega} \frac{\alpha^2 F(\omega')}{\omega'} d\omega', \tag{2}$$

where $\lambda(\omega_{\max})$ is the maximum phonon frequency and λ is the electron–phonon coupling constant λ utilized in Eq. (1). Moreover, the characteristic phonon frequency $\omega_{\log}$, which is logarithmically averaged, can be expressed as

$$\omega_{\log} = \exp\left[\frac{2}{\lambda}\int \frac{d\omega}{\omega}\alpha^2 F(\omega)\ln\,\omega\right]. \tag{3}$$

The following are the isotropic Migdal–Eliashberg equations:[2,42]

$$Z(i\omega_n) = 1 + \frac{\pi T}{\omega_n}\sum_{n'} \frac{\omega_{n'}}{\sqrt{\omega_n^2 + \Delta^2(i\omega_n)}} \times \lambda(n-n'), \tag{4}$$

$$Z(i\omega_n)\Delta(i\omega_n) = \pi T\sum_{n'} \int \frac{\Delta(i\omega_{n'})}{\sqrt{\omega_n^2 + \Delta^2(i\omega_n)}} \times \left[\lambda(n-n') - \mu^*\right], \tag{5}$$

where the superconducting gap $\Delta(i\omega_n)$ and the fermionic Matsubara frequencies $\omega_{n'}$ are represented, together with the renormalization function $Z(i\omega_n)$. Consequently, the definition of the Eliashberg spectral function is

$$\alpha^2 F(\omega) = \frac{1}{2\pi N(0)}\sum_{qj} \frac{\gamma_{qj}}{\omega_{qj}} \delta(\hbar\omega - \hbar\omega_{qj}), \tag{6}$$

where ω_{qj} denotes frequency with a phonon j and a wave vector q, and γ_{qj} denotes phonon linewidth.

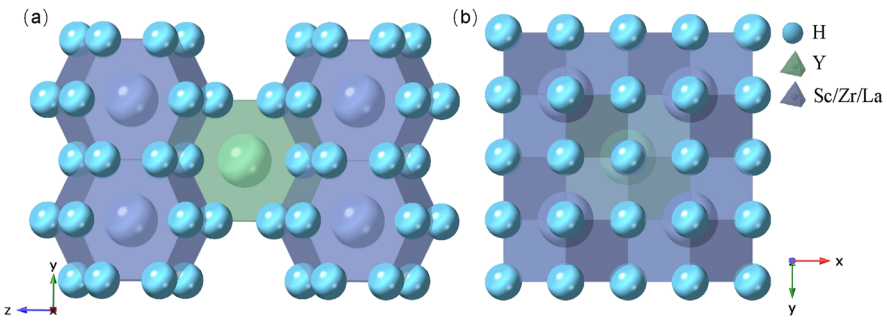

FIG. 1. Crystal structure representations of (Y,Sc)H_4 at 100 GPa, (Y,Zr)H_4 at 200 GPa, and (Y,La)H_4 at 120 GPa. The structures of (Y,Sc,Zr,La)H_4 are depicted in (a) front and (b) side views. The blue spheres represent hydrogen (H), the green spheres represent Y, and the purple spheres represent Sc, Zr, or La.

III. RESULTS AND DISCUSSION

As the matrix material investigated in this study, YH_4 crystallizes in the $I4/mmm$ space group (No. 139), exhibiting an experimental superconducting transition temperature (T_c) of ~88 K at 155 GPa,[45] while theoretical predictions estimate T_c between 84 and 95 K at 120 GPa.[44] The $(Y,Sc)H_4$, $(Y,Zr)H_4$ and $(Y,La)H_4$ compounds maintain structural stability at 100, 200, and 120 GPa, respectively, crystallizing in the same space group as YH_4, as shown in Figs. 1(a) and 1(b). Complete structural modeling parameters and thorough analyses of both kinetic and thermodynamic stability for $(Y,Sc)H_4$ (100 GPa), $(Y,Zr)H_4$ (200 GPa), and $(Y,La)H_4$ (120 GPa) systems are presented in Figs. S2–S4. The optimized lattice constants are as follows: for $(Y,Sc)H_4$, a = b = 2.856 Å, c = 5.114 Å; for $(Y,Zr)H_4$, a = b = 2.678 Å, c = 5.056 Å; for $(Y,La)H_4$, a = b = 2.811 Å, c = 5.648 Å. Each structure consists of a cage of 18 hydrogen atoms enclosing the heavier metal atoms (Y, Sc, La, or Zr). These materials share the same structure as other MH_4 compounds (M representing different metal elements),[46] including pure YH_4,[44,45] ScH_4,[19,46–48] ZrH_4,[46,49] and LaH_4.[26] Interestingly, hydrogen compounds composed of Y (group IIIB) and Zr (group IVB) require higher pressures to stabilize, despite their similar elemental weights. However, hydrides with elements Y, Sc, or La from group IIIB can stabilize at comparatively lower pressures.

Figure 2 shows the differential charge density and average Y–H bond lengths for $(Y,Sc)H_4$, $(Y,La)H_4$, and $(Y,Zr)H_4$, while Fig. S5 presents the electron localization function (ELF) maps along the (110) plane. Interestingly, we find that some electrons detached from the central atoms (Sc, Zr, and La) become highly localized in the interstitial regions near hydrogen sites. This electron distribution closely resembles that of the near-room-temperature superconductor LaH_{10},[50] suggesting a possible link to high-T_c behavior. Furthermore, distinct bonding characteristics are observed across the three compounds, which critically influence their electronic structures and likely govern their superconducting properties.

$(Y,Sc)H_4$, stabilized at a relatively low pressure of 100 GPa, exhibits the strongest charge redistribution and highly localized covalent Y–H bonds, with ELF values approaching 1 and the longest average Y–H bond length (2.06 Å). This indicates that the strong electron–phonon coupling is closely associated with the material's bonding framework, which is enhanced under compression, rather than being purely a consequence of external pressure. In contrast, $(Y,Zr)H_4$ requires a much higher pressure of 200 GPa to stabilize, yet shows the weakest charge redistribution and lowest ELF values. Its shortest Y–H bond length (1.92 Å) suggests a more compact but less covalent bonding environment. The structural rigidity introduced by Zr likely suppresses bond flexibility and electron localization, thus weakening electron–phonon coupling.

At an intermediate stabilization pressure of 120 GPa, $(Y,La)H_4$ demonstrates intermediate charge redistribution characteristics accompanied by partial electron localization, featuring an average Y–H bond distance of 2.01 Å. The larger ionic radius and lower electro-negativity of La may lead to a more relaxed bonding environment that offsets pressure-induced bond compression. The superconducting potential of these hydrides depends more critically on the nature of hydrogen-mediated covalent bonding and electron localization than on the applied pressure. Among them, $(Y,Sc)H_4$ stands out as a promising candidate due to its favorable bonding characteristics maintained even at low pressure.

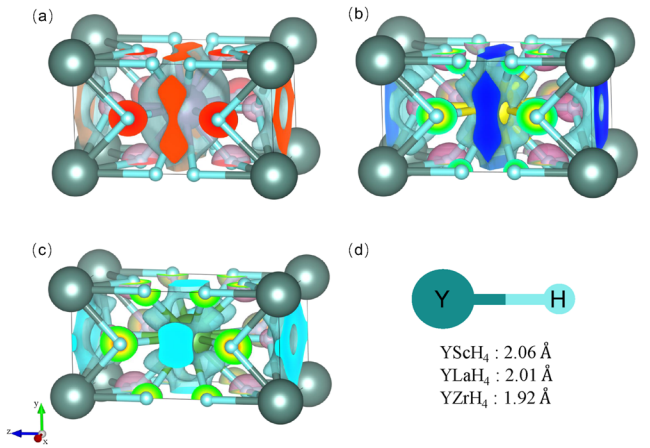

FIG. 2. Front views of the differential charge densities are shown for (a) $(Y,Sc)H_4$, (b) $(Y,Zr)H_4$, and (c) $(Y,La)H_4$. Small light blue spheres represent hydrogen (H), large dark cyan spheres represent yttrium (Y), and the large pink, yellow, and light green spheres at the center represent Sc, Zr, and La, respectively. Negative charge regions are depicted in blue, while positive charge regions are shown in pink. (d) The average bond lengths between Y and H elements for the three materials.

Figures 3(a), 3(f), and 3(k) depict the electronic band structures with orbital resolution of $(Y,Sc)H_4$(100 GPa), $(Y,Zr)H_4$(200 GPa), and $(Y,La)H_4$(120 GPa), respectively. Combined with the electronic density of states (EDOS) for $(Y,Sc)H_4$ at 100 GPa, as shown in Fig. 3(b), the total EDOS value is ~1 state/eV. The contributions from various orbitals H-*s*, Sc-*s*, Sc-*p*, Sc-*d*, Y-*s*, Y-*p*, and Y-*d* are represented by light-green, dark-red, dark-blue, light-blue, dark-yellow, dark-violet, and mauve dots, respectively. Moreover, Fig. 3(a) reveals that the electronic bands near the Fermi level for $(Y,Sc)H_4$ are predominantly composed of Y-*d*, Sc-*d*, and the H-*s* orbitals.

Since both La and Sc belong to group IIIB, the electronic bands in Figs. 3(a) and 3(k) are similar. Sc has $3d^1$ valence electrons, while La has $5d^1$ valence electrons, resulting in a higher Fermi level for $(Y,La)H_4$ compared to $(Y,Sc)H_4$. In contrast, the electronic bands of $(Y,Zr)H_4$, depicted in Fig. 3(f), differ significantly from the other two materials. This is because Zr, a member of group IVB, has $4d^2$ valence electrons, meaning one more than the valence electrons of Sc and La.

Figure 3(f) illustrates the orbital contributions near the Fermi level for $(Y,Zr)H_4$ at 200 GPa, where Zr-*d*, Y-*d*, and H-*s* orbitals dominate the electronic bands. Similarly, the electronic bands near the Fermi level for $(Y,La)H_4$, as shown in Fig. 3(k), are primarily composed of H-*s*, La-*d*, and a smaller contribution from Y-*d* orbitals. Figures 3(g) and 3(l) show that the total electronic density of states (EDOS) at the Fermi level (E_F) is ~0.9 states/eV for $(Y,Zr)H_4$ and 0.94 states/eV for $(Y,La)H_4$. Both values are lower than the EDOS of $(Y,Sc)H_4$, which accounts for its higher T_c. The enhanced T_c of $(Y,Sc)H_4$ is thus correlated with the greater EDOS amplitude around E_F.

The phonon dispersions of $(Y,Sc)H_4$, $(Y,Zr)H_4$, and $(Y,La)H_4$ are presented in Figs. 3(c), 3(h), and 3(m), respectively,

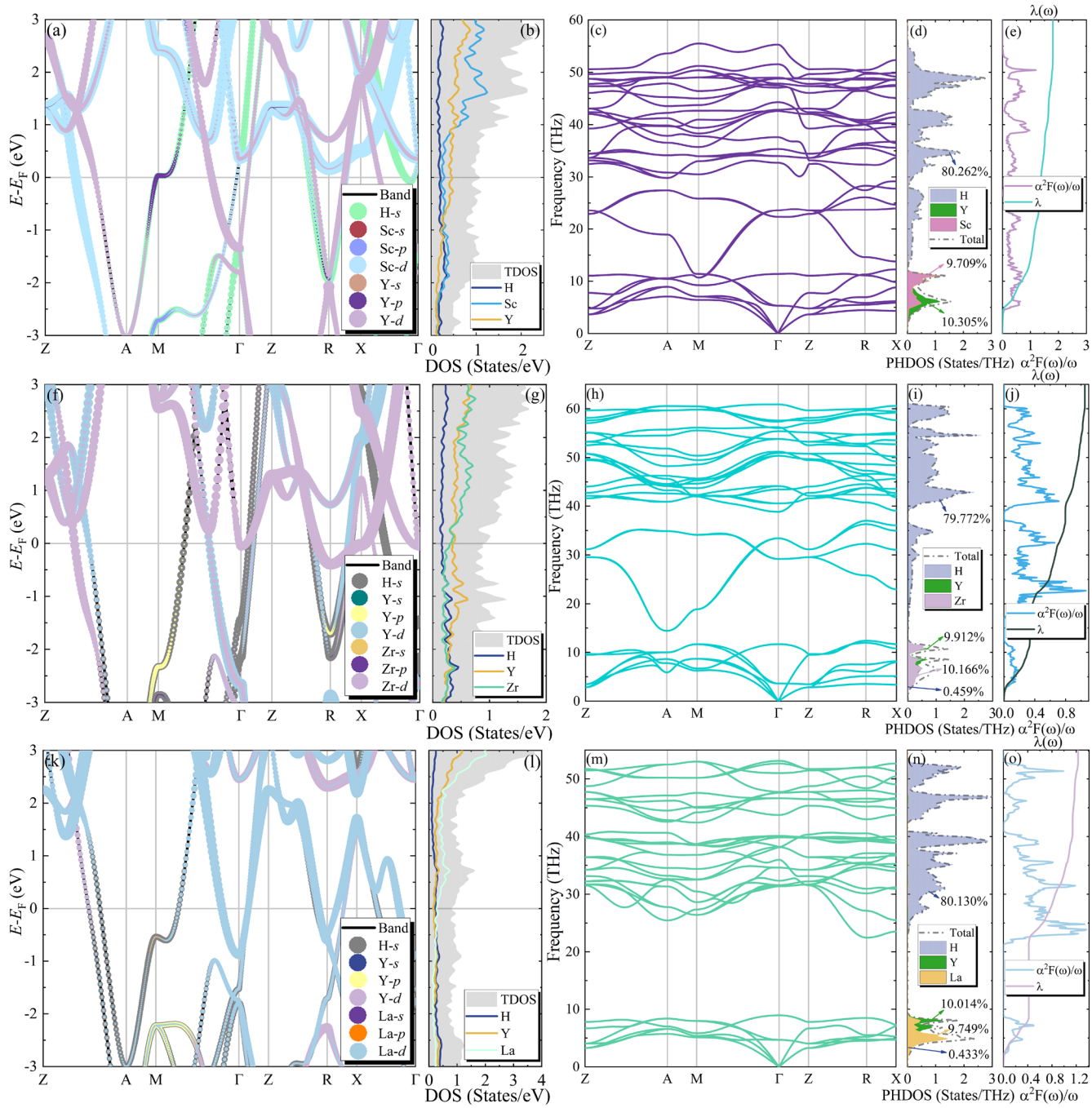

FIG. 3. Electronic and phonon properties of $(Y,Sc)H_4$ (100 GPa), $(Y,Zr)H_4$ (200 GPa), and $(Y,La)H_4$ (120 GPa), respectively. (a) The electronic band structures and (b) the electronic density of states (EDOS) for $(Y,Sc)H_4$. The gray-scale highlights orbital contributions, with H, Sc, and Y orbitals represented by dark blue, light blue, and orange lines, respectively. (c) The phonon dispersion and (d) phonon density of states (PDOS) for $(Y,Sc)H_4$, where H, Y, and Sc are represented by dark blue, green, and pink shades. The total PDOS is shown as a gray dotted line, with arrows indicating the percentage of PDOS contributed by each element. (e) The electron–phonon coupling integral $\lambda(\omega)$ (aqua line) and the Eliashberg spectral function $\alpha^2F(\omega)$ (violet line). (f)–(j) and (k)–(o) depict the corresponding properties for $(Y,Zr)H_4$ and $(Y,La)H_4$, respectively.

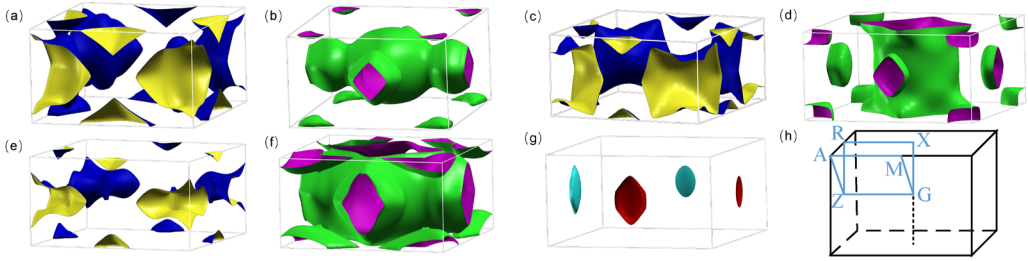

FIG. 4. Calculated Fermi surfaces for $(Y,Sc)H_4$, $(Y,La)H_4$, and $(Y,Zr)H_4$. Panels (a) and (b) show the first and second energy bands of $(Y,Sc)H_4$, while panels (c) and (d) depict the first and second energy bands of $(Y,La)H_4$. Panels (e), (f), and (g) illustrate the first, second, and third energy bands of $(Y,Zr)H_4$, respectively, as generated using Xcrysden.[51] (h) The *k*-path, comprising high-symmetry points Z, A, M, Γ, R, and X, is represented by blue lines in the panel.

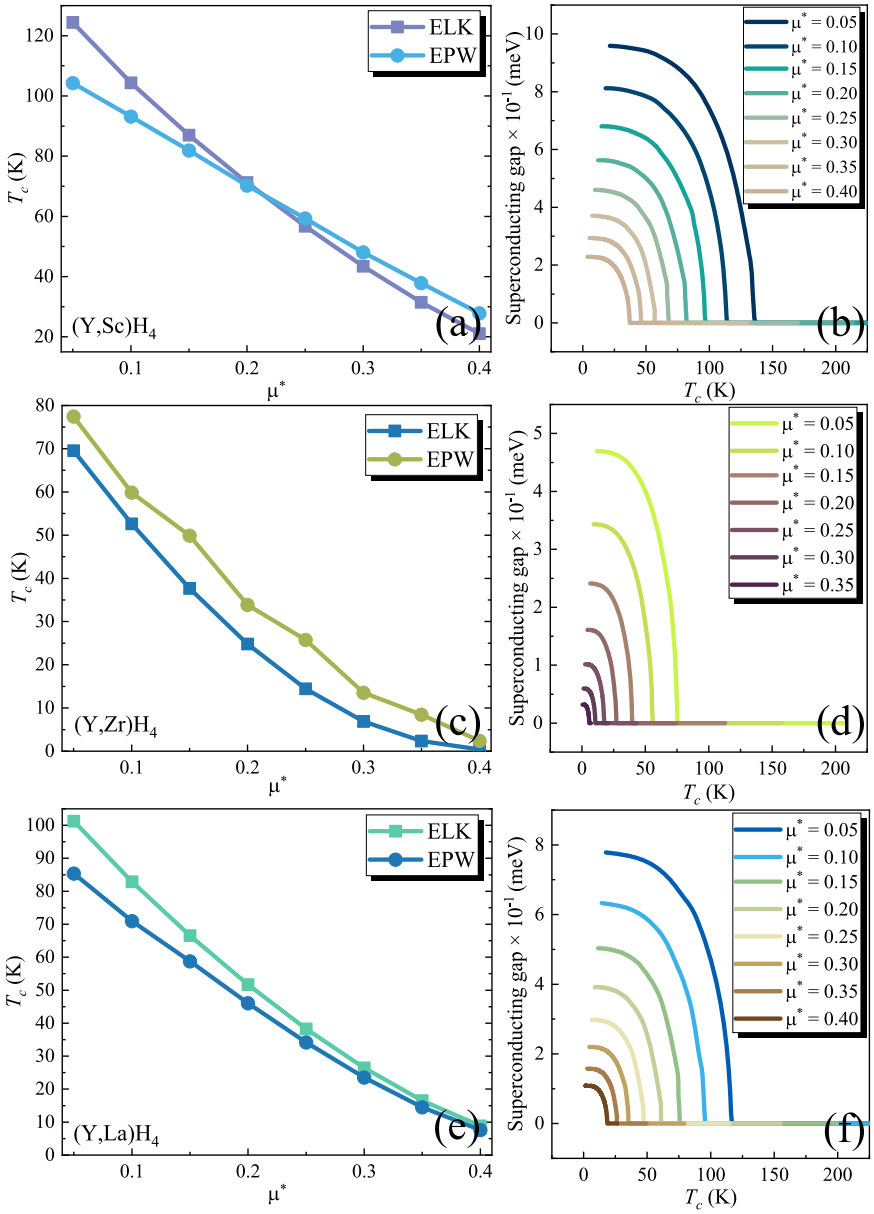

FIG. 5. Superconducting characteristics of $(Y,Sc)H_4$, $(Y,Zr)H_4$, and $(Y,La)H_4$. The dark purple, dark blue, and green curves in panels (a), (c), and (e) represent the calculated T_c values using the ELK code[41] with μ^* ranging from 0.05 to 0.40, while the light blue, yellow, and denim blue curves in the same panels correspond to the T_c values computed using the EPW code,[39] as detailed in panels (b), (d), and (f), respectively.

demonstrating the dynamical stability of these materials. Notably, the gap between the optical and acoustic branches increases across Figs. 3(c), 3(h), and 3(m). At high frequencies, hydrogen dominates the optical branches, while the metallic elements Y, Sc, La, and Zr contribute predominantly to the acoustic branches at low frequencies, as illustrated in Figs. 3(d), 3(i), and 3(n). The phonon density of states (PDOS) shows that Sc, Zr, and La occupy nearly the same proportion. Further calculations for $(Y,Sc)H_4$, $(Y,Zr)H_4$, and $(Y,La)H_4$ yield the Eliashberg spectral function $\alpha^2F(\omega)$ and the electron–phonon coupling $\lambda(\omega)$, depicted in Figs. 3(e), 3(j), and 3(o).

Interestingly, the electron–phonon coupling strength λ and spectral functions for $(Y,Zr)H_4$ and $(Y,La)H_4$ indicate that high-frequency phonons play a critical role in the superconducting properties of both materials. These high-frequency phonons, represented by the optical branches, are predominantly contributed by the hydrogen (H) atoms, as shown in Figs. 3(h) and 3(m). In contrast, an important distinction for $(Y,Sc)H_4$ is the absence of a gap between the acoustic and optical branches, as observed by comparing Figs. 3(c) and 3(e). The λ values for $(Y,Sc)H_4$, $(Y,Zr)H_4$, and $(Y,La)H_4$ are 1.80, 1.05, and 1.23, respectively, further highlighting the enhanced electron–phonon coupling in $(Y,Sc)H_4$.

As shown in Fig. 4, the Fermi surface (FS) topologies of $(Y,Sc)H_4$, $(Y,Zr)H_4$, and $(Y,La)H_4$ differ markedly, reflecting distinct orbital contributions and symmetry-derived band degeneracies. These topological features directly correlate with the band structures and electron–phonon coupling constants (λ) extracted from Fig. 3, highlighting the critical role of electronic structure in determining superconducting properties. In $(Y,Sc)H_4$, the Fermi surface consists of a three-dimensional, highly interconnected network formed by degenerate E_g bands, primarily originating from Y or Sc-*d* orbitals crossing the Fermi level along high-symmetry directions such as Γ–Z and R–A. This topology promotes strong electronic state overlap and scattering phase space, resulting in a substantial electron–phonon coupling constant of $\lambda = 1.80$, indicative of strong superconducting potential.

In contrast, $(Y,La)H_4$ exhibits a quasi-two-dimensional Fermi surface composed of cylindrical sheets primarily derived from the *d* orbitals of Y, with minimal dispersion along the k_z direction. Although the band remains degenerate, the reduced interlayer electronic overlap and stronger anisotropy yield a moderately strong coupling of $\lambda = 1.23$. Meanwhile, $(Y,Zr)H_4$ presents a collection of discrete, nearly spherical and spindle-shaped Fermi pockets spread across the Brillouin zone, arising from hybridized Zr-*d* and Y or Zr-*d* orbitals. This fragmented and weakly connected Fermi surface leads to a lower density of states at the Fermi level and a relatively weak electron–phonon interaction, with $\lambda = 1.05$. The dimensionality, degeneracy, and multiplicity of Fermi surface sheets substantially modulate the electronic density of states and electron–phonon coupling strength, ultimately governing the superconducting transition temperature achievable in each compound. In addition, Fig. 4(h) highlights the high-symmetry point pathways for the three materials.

Two methods were employed to systematically determine the superconducting properties of $(Y,Sc)H_4$, $(Y,Zr)H_4$, and $(Y,La)H_4$, as shown in Fig. 5. The computational details are outlined in Eqs. (1), (4), and (5). Using the EPW code,[39] the critical temperature T_c as a function of the Coulomb pseudopotential parameter μ^* was calculated, with results displayed in Figs. 5(a), 5(c), and 5(e). To investigate the T_c of $(Y,Sc)H_4$, $(Y,Zr)H_4$, and $(Y,La)H_4$ systems, we selected $\mu^* = 0.05$ in our EPW calculations. This value was determined based on the experimentally measured T_c of 90 K for $(Y,La)H_4$ at 110 GPa from previous studies.[52]

Once the computational parameters were established, T_c values for the two materials were calculated using the EPW code[39] to be 104.32, 77.40, and 85.39 K at 100, 200, and 120 GPa, respectively. As shown in Figs. 5(b), 5(d), and 5(f), T_c values obtained using the ELK[41] program exhibit the same decreasing trend with increasing μ^* as observed with the EPW code. Assuming $\mu^* = 0.05$, the calculated T_c values are 124.43 K for $(Y,Sc)H_4$, 69.55 K for $(Y,Zr)H_4$, and 101.24 K for $(Y,La)H_4$. The two computational approaches yield consistent results, indicating the credibility of our findings on the superconducting properties of these materials.

After systematically evaluating two computational approaches, we ultimately selected the ELK[41] code results for final reporting due to their optimal balance between computational efficiency and predictive accuracy. While the superconducting transition temperature (T_c) of $(Y,La)H_4$ has been previously documented,[52] our calculations predict that $(Y,Sc)H_4$ at 100 GPa exhibits a significantly enhanced T_c of 124.43 K. This theoretical prediction, representing a notable advancement beyond currently reported values, awaits experimental verification through future high-pressure studies.

To compare the T_c of binary hydrides in the *I*4/*mmm* space group under varying pressure conditions, we compiled their data alongside our results, as shown in Fig. 6. In the field of superconductivity, the ideal materials exhibit higher T_c under lower pressures. As illustrated in Fig. 6, the T_c for $(Y,Sc)H_4$ in this study, 124.43 K, establishes it as the best-performing superconductor among binary hydrides in the *I*4/*mmm* space group. Our findings indicate that $(Y,Sc,La)H_4$ outperforms pure YH_4,[44,45] ScH_4,[19,46–48] and LaH_4.[26]

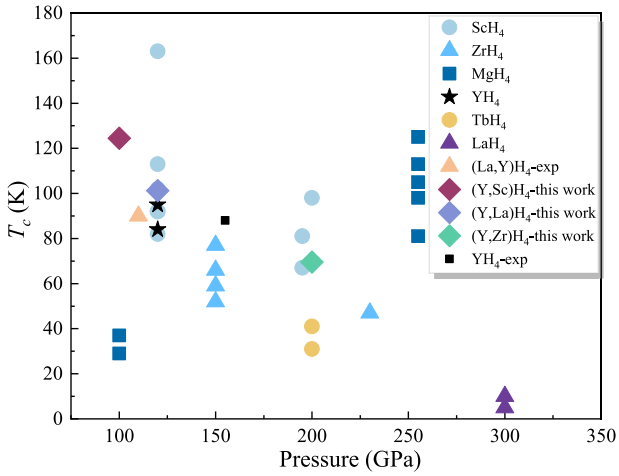

FIG. 6. Critical temperature T_c of MH_4 compounds (M represents different metal elements) with the *I*4/*mmm* space group at various pressures. The red, purple, and green rhombuses indicate T_c values for $(Y,Sc)H_4$, $(Y,Zr)H_4$, and $(Y,La)H_4$, respectively. Light blue dots, bright blue triangles, navy blue squares, black stars, orange dots, purple triangles, and pink triangles represent data for ScH_4,[19,46–48] ZrH_4,[46,49] MgH_4,[46,49,53] YH_4,[44,45] TbH_4,[54] LaH_4,[26] and $(La,Y)H_4$,[52] respectively.

Conversely, $(Y,Zr)H_4$ exhibits a significantly lower T_c compared to other compounds in the same family. Based on these results, we conclude that metallic elements can be incorporated into binary hydride superconductors to enhance T_c and reduce the required pressure. A particularly effective strategy involves substituting a metal element from the same group, while substitution with neighboring elements significantly degrades the superconducting performance of the materials.

IV. CONCLUSIONS AND DISCUSSIONS

In this work, we determined the precise superconducting critical temperatures T_c for $(Y,Sc)H_4$ (100 GPa), $(Y,Zr)H_4$ (200 GPa), and $(Y,La)H_4$ (120 GPa) by substituting Sc, Zr, and La for half of the Y atoms, using three computational codes. In addition, we calculated electronic band structures, phonon dispersions, electron–phonon coupling strengths, and superconducting properties based on the McMillan–Allen–Dynes formula, as well as the isotropic and anisotropic Migdal–Eliashberg equations. Our key findings are summarized as follows:

(i) For $(Y,Sc)H_4$ (100 GPa), $(Y,Zr)H_4$ (200 GPa), and $(Y,La)H_4$ (120 GPa), the T_c values are 124.43, 69.55, and 101.24 K, respectively, when $\mu^* = 0.05$.
(ii) The excellent superconductivity of $(Y,Sc,Zr,La)H_4$ can be attributed to the critical contribution of the lowest phonon branches.
(iii) The strong electron–phonon coupling in $(Y,Sc)H_4$ arises from a combination of soft hydrogen-dominated phonon modes, strong covalent bonding between hydrogen and metal atoms, and electron localization in interstitial regions.
(iv) Doping with isovalent metals enhances T_c, while adjacent-element doping degrades superconducting performance.

SUPPLEMENTARY MATERIAL

See the supplementary material for unit cell construction in Sc-, La-, and Zr-substituted systems, pressure selection criteria, and dynamic and thermodynamic stability analysis of $(Y,Sc)H_4$, $(Y,Zr)H_4$, and $(Y,La)H_4$. The electron localization function (ELF) plots at corresponding pressures are also presented.

ACKNOWLEDGMENTS

The authors gratefully acknowledge discussions with Zhen Tong about the EPW code and Wenbo Zhao about the ELK code. We acknowledge the support from the National Natural Science Foundation of China (Grant Nos. 12104356 and 52250191). This work is sponsored by the Key Research and Development Program of the Ministry of Science and Technology (Grant No. 2023YFB4604100). We also acknowledge the support from the HPC Platform, Xi'an Jiaotong University.

AUTHOR DECLARATIONS

Conflict of Interest

The authors have no conflicts to disclose.

Author Contributions

Xuejie Li: Investigation (lead); Methodology (lead); Software (lead); Validation (lead); Visualization (lead); Writing – original draft (lead). **Yuzhou Hao**: Investigation (supporting). **Yujie Liu**: Investigation (supporting). **Xiaoying Wang**: Investigation (supporting). **Turab Lookman**: Writing – review & editing (supporting). **Jun Sun**: Writing – review & editing (supporting). **Xiangdong Ding**: Writing – review & editing (supporting). **Zhibin Gao**: Writing – review & editing (lead).

DATA AVAILABILITY

The data that support the findings of this study are available within the article and its supplementary material.

REFERENCES

[1] L. Boeri, R. Hennig, P. Hirschfeld, G. Profeta, A. Sanna, E. Zurek, W. E. Pickett, M. Amsler, R. Dias, M. I. Eremets, C. Heil, R. J. Hemley, H. Liu, Y. Ma, C. Pierleoni, A. N. Kolmogorov, N. Rybin, D. Novoselov, V. Anisimov, A. R. Oganov, C. J. Pickard, T. Bi, R. Arita, I. Errea, C. Pellegrini, R. Requist, E. K. U. Gross, E. R. Margine, S. R. Xie, Y. Quan, A. Hire, L. Fanfarillo, G. R. Stewart, J. J. Hamlin, V. Stanev, R. S. Gonnelli, E. Piatti, D. Romanin, D. Daghero, and R. Valenti, "The 2021 room-temperature superconductivity roadmap," J. Phys.: Condens. Matter **34**, 183002 (2022).
[2] K. P. Hilleke and E. Zurek, "Tuning chemical precompression: Theoretical design and crystal chemistry of novel hydrides in the quest for warm and light superconductivity at ambient pressures," J. Appl. Phys. **131**, 070901 (2022).
[3] M. Du, W. Zhao, T. Cui, and D. Duan, "Compressed superhydrides: The road to room temperature superconductivity," J. Phys.: Condens. Matter **34**, 173001 (2022).
[4] A. P. Drozdov, M. I. Eremets, I. A. Troyan, V. Ksenofontov, and S. I. Shylin, "Conventional superconductivity at 203 kelvin at high pressures in the sulfur hydride system," Nature **525**, 73–76 (2015).
[5] D. Duan, Y. Liu, F. Tian, D. Li, X. Huang, Z. Zhao, H. Yu, B. Liu, W. Tian, and T. Cui, "Pressure-induced metallization of dense $(H_2S)_2H_2$ with high-T_c superconductivity," Sci. Rep. **4**, 6968 (2014).
[6] P. Bhattacharyya, W. Chen, X. Huang, S. Chatterjee, B. Huang, B. Kobrin, Y. Lyu, T. J. Smart, M. Block, E. Wang *et al.*, "Imaging the Meissner effect in hydride superconductors using quantum sensors," Nature **627**, 73–79 (2024).
[7] Y. Song, J. Bi, Y. Nakamoto, K. Shimizu, H. Liu, B. Zou, G. Liu, H. Wang, and Y. Ma, "Stoichiometric ternary superhydride $LaBeH_8$ as a new template for high-temperature superconductivity at 110 K under 80 GPa," Phys. Rev. Lett. **130**, 266001 (2023).
[8] D. V. Semenok, A. G. Kvashnin, A. G. Ivanova, V. Svitlyk, V. Y. Fominski, A. V. Sadakov, O. A. Sobolevskiy, V. M. Pudalov, I. A. Troyan, and A. R. Oganov, "Superconductivity at 161 K in thorium hydride ThH_{10}: Synthesis and properties," Mater. Today **33**, 36–44 (2020).
[9] M. Shao, S. Chen, W. Chen, K. Zhang, X. Huang, and T. Cui, "Superconducting ScH_3 and LuH_3 at megabar pressures," Inorg. Chem. **60**, 15330–15335 (2021).
[10] L.-C. Chen, T. Luo, Z.-Y. Cao, P. Dalladay-Simpson, G. Huang, D. Peng, L.-L. Zhang, F. A. Gorelli, G.-H. Zhong, H.-Q. Lin, and X.-J. Chen, "Synthesis and superconductivity in yttrium-cerium hydrides at high pressures," Nat. Commun. **15**, 1809 (2024).
[11] P. Kong, V. S. Minkov, M. A. Kuzovnikov, A. P. Drozdov, S. P. Besedin, S. Mozaffari, L. Balicas, F. F. Balakirev, V. B. Prakapenka, S. Chariton, D. A. Knyazev, E. Greenberg, and M. I. Eremets, "Superconductivity up to 243 K in the yttrium-hydrogen system under high pressure," Nat. Commun. **12**, 5075 (2021).
[12] I. A. Troyan, D. V. Semenok, A. G. Kvashnin, A. V. Sadakov, O. A. Sobolevskiy, V. M. Pudalov, A. G. Ivanova, V. B. Prakapenka, E. Greenberg, A. G. Gavriliuk, I. S. Lyubutin, V. V. Struzhkin, A. Bergara, I. Errea, R. Bianco, M. Calandra, F. Mauri, L. Monacelli, R. Akashi, and A. R. Oganov, "Anomalous high-temperature superconductivity in YH_6," Adv. Mater. **33**, 2006832 (2021).

[13]W. Chen, D. V. Semenok, X. Huang, H. Shu, X. Li, D. Duan, T. Cui, and A. R. Oganov, "High-temperature superconducting phases in cerium superhydride with a T_c up to 115 K below a pressure of 1 megabar," Phys. Rev. Lett. **127**, 117001 (2021).
[14]J. Nagamatsu, N. Nakagawa, T. Muranaka, Y. Zenitani, and J. Akimitsu, "Superconductivity at 39 K in magnesium diboride," Nature **410**, 63–64 (2001).
[15]V. S. Minkov, S. L. Bud'ko, F. F. Balakirev, V. B. Prakapenka, S. Chariton, R. J. Husband, H. P. Liermann, and M. I. Eremets, "Magnetic field screening in hydrogen-rich high-temperature superconductors," Nat. Commun. **13**, 3194 (2022).
[16]R. Lucrezi, P. P. Ferreira, S. Hajinazar, H. Mori, H. Paudyal, E. R. Margine, and C. Heil, "Full-bandwidth anisotropic migdal-eliashberg theory and its application to superhydrides," Commun. Phys. **7**, 33 (2024).
[17]Y. Yao, J. S. Tse, Y. Ma, and K. Tanaka, "Superconductivity in high-pressure SiH_4," Europhys. Lett. **78**, 37003 (2007).
[18]P. Hou, X. Zhao, F. Tian, D. Li, D. Duan, Z. Zhao, B. Chu, B. Liu, and T. Cui, "High pressure structures and superconductivity of $AlH_3(H_2)$ predicted by first principles," RSC Adv. **5**, 5096–5101 (2015).
[19]X. Ye, N. Zarifi, E. Zurek, R. Hoffmann, and N. W. Ashcroft, "High hydrides of scandium under pressure: Potential superconductors," J. Phys. Chem. C **122**, 6298–6309 (2018).
[20]Y. Fu, X. Du, L. Zhang, F. Peng, M. Zhang, C. J. Pickard, R. J. Needs, D. J. Singh, W. Zheng, and Y. Ma, "High-pressure phase stability and superconductivity of pnictogen hydrides and chemical trends for compressed hydrides," Chem. Mater. **28**, 1746–1755 (2016).
[21]F. Peng, Y. Sun, C. J. Pickard, R. J. Needs, Q. Wu, and Y. Ma, "Hydrogen clathrate structures in rare earth hydrides at high pressures: Possible route to room-temperature superconductivity," Phys. Rev. Lett. **119**, 107001 (2017).
[22]X.-L. He, W. Zhao, Y. Xie, A. Hermann, R. J. Hemley, H. Liu, and Y. Ma, "Predicted hot superconductivity in $LaSc_2H_{24}$ under pressure," Proc. Natl. Acad. Sci. U. S. A. **121**, e2401840121 (2024).
[23]D. V. Semenok, A. G. Kvashnin, I. A. Kruglov, and A. R. Oganov, "Actinium hydrides AcH_{10}, AcH_{12}, and AcH_{16} as high-temperature conventional superconductors," J. Phys. Chem. Lett. **9**, 1920–1926 (2018).
[24]X. Zhong, Y. Sun, T. Iitaka, M. Xu, H. Liu, R. J. Hemley, C. Chen, and Y. Ma, "Prediction of above-room-temperature superconductivity in lanthanide/actinide extreme superhydrides," J. Am. Chem. Soc. **144**, 13394–13400 (2022).
[25]W. Sun, X. Kuang, H. D. J. Keen, C. Lu, and A. Hermann, "Second group of high-pressure high-temperature lanthanide polyhydride superconductors," Phys. Rev. B **102**, 144524 (2020).
[26]H. Liu, I. I. Naumov, R. Hoffmann, N. W. Ashcroft, and R. J. Hemley, "Potential high-T_c superconducting lanthanum and yttrium hydrides at high pressure," Proc. Natl. Acad. Sci. U. S. A. **114**, 6990–6995 (2017).
[27]X. Liang, A. Bergara, L. Wang, B. Wen, Z. Zhao, X.-F. Zhou, J. He, G. Gao, and Y. Tian, "Potential high-T_c superconductivity in $CaYH_{12}$ under pressure," Phys. Rev. B **99**, 100505 (2019).
[28]H. Xie, D. Duan, Z. Shao, H. Song, Y. Wang, X. Xiao, D. Li, F. Tian, B. Liu, and T. Cui, "High-temperature superconductivity in ternary clathrate $YCaH_{12}$ under high pressures," J. Phys.: Condens. Matter **31**, 245404 (2019).
[29]X. Liu, X. Huang, P. Song, C. Wang, L. Zhang, P. Lv, L. Liu, W. Zhang, J.-H. Cho, and Y. Jia, "Strong electron-phonon coupling superconductivity in compressed α-MoB_2 induced by double Van Hove singularities," Phys. Rev. B **106**, 064507 (2022).
[30]J. Bekaert, M. Petrov, A. Aperis, P. M. Oppeneer, and M. V. Milošević, "Hydrogen-induced high-temperature superconductivity in two-dimensional materials: The example of hydrogenated monolayer MgB_2," Phys. Rev. Lett. **123**, 077001 (2019).
[31]W. Chen, X. Huang, D. V. Semenok, S. Chen, D. Zhou, K. Zhang, A. R. Oganov, and T. Cui, "Enhancement of superconducting properties in the La–Ce–H system at moderate pressures," Nat. Commun. **14**, 2660 (2023).
[32]G. Kresse and J. Furthmüller, "Efficiency of ab-initio total energy calculations for metals and semiconductors using a plane-wave basis set," Comp. Mater. Sci. **6**, 15–50 (1996).
[33]G. Kresse and J. Furthmüller, "Efficient iterative schemes for *ab initio* total-energy calculations using a plane-wave basis set," Phys. Rev. B **54**, 11169–11186 (1996).
[34]J. P. Perdew, K. Burke, and M. Ernzerhof, "Generalized gradient approximation made simple," Phys. Rev. Lett. **77**, 3865–3868 (1996).
[35]J. A. White and D. M. Bird, "Implementation of gradient-corrected exchange-correlation potentials in car-parrinello total-energy calculations," Phys. Rev. B **50**, 4954–4957 (1994).
[36]Z. Wu and R. E. Cohen, "More accurate generalized gradient approximation for solids," Phys. Rev. B **73**, 235116 (2006).
[37]P. Giannozzi, S. Baroni, N. Bonini, M. Calandra, R. Car, C. Cavazzoni, D. Ceresoli, G. L. Chiarotti, M. Cococcioni, I. Dabo, A. Dal Corso, S. de Gironcoli, S. Fabris, G. Fratesi, R. Gebauer, U. Gerstmann, C. Gougoussis, A. Kokalj, M. Lazzeri, L. Martin-Samos, N. Marzari, F. Mauri, R. Mazzarello, S. Paolini, A. Pasquarello, L. Paulatto, C. Sbraccia, S. Scandolo, G. Sclauzero, A. P. Seitsonen, A. Smogunov, P. Umari, and R. M. Wentzcovitch, "QUANTUM ESPRESSO: A modular and open-source software project for quantum simulations of materials," J. Phys.: Condens. Matter **21**, 395502 (2009).
[38]M. J. van Setten, M. Giantomassi, E. Bousquet, M. J. Verstraete, D. R. Hamann, X. Gonze, and G.-M. Rignanese, "The PSEUDODOJO: Training and grading a 85 element optimized norm-conserving pseudopotential table," Comput. Phys. Commun. **226**, 39–54 (2018).
[39]P. Giannozzi, O. Andreussi, T. Brumme, O. Bunau, M. Buongiorno Nardelli, M. Calandra, R. Car, C. Cavazzoni, D. Ceresoli, M. Cococcioni, N. Colonna, I. Carnimeo, A. Dal Corso, S. de Gironcoli, P. Delugas, R. A. DiStasio, A. Ferretti, A. Floris, G. Fratesi, G. Fugallo, R. Gebauer, U. Gerstmann, F. Giustino, T. Gorni, J. Jia, M. Kawamura, H.-Y. Ko, A. Kokalj, E. Küçükbenli, M. Lazzeri, M. Marsili, N. Marzari, F. Mauri, N. L. Nguyen, H.-V. Nguyen, A. Otero de-la Roza, L. Paulatto, S. Poncé, D. Rocca, R. Sabatini, B. Santra, M. Schlipf, A. P. Seitsonen, A. Smogunov, I. Timrov, T. Thonhauser, P. Umari, N. Vast, X. Wu, and S. Baroni, "Advanced capabilities for materials modelling with QUANTUM ESPRESSO," J. Phys.: Condens. Matter **29**, 465901 (2017).
[40]E. R. Margine and F. Giustino, "Anisotropic Migdal-Eliashberg theory using Wannier functions," Phys. Rev. B **87**, 024505 (2013).
[41]See http://elk.sourceforge.net/ for The Elk Code.
[42]J. A. Flores-Livas, L. Boeri, A. Sanna, G. Profeta, R. Arita, and M. Eremets, "A perspective on conventional high-temperature superconductors at high pressure: Methods and materials," Phys. Rep. **856**, 1–78 (2020).
[43]P. B. Allen and R. C. Dynes, "Transition temperature of strong-coupled superconductors reanalyzed," Phys. Rev. B **12**, 905–922 (1975).
[44]M. Shao, W. Chen, K. Zhang, X. Huang, and T. Cui, "High-pressure synthesis of superconducting clathratelike YH_4," Phys. Rev. B **104**, 174509 (2021).
[45]Y. Li, J. Hao, H. Liu, J. S. Tse, Y. Wang, and Y. Ma, "Pressure-stabilized superconductive yttrium hydrides," Sci. Rep. **5**, 9948 (2015).
[46]T. Bi and E. Zurek, "Electronic structure and superconductivity of compressed metal tetrahydrides," Chem. - Eur. J. **27**, 14858–14870 (2021).
[47]K. Abe, "Hydrogen-rich scandium compounds at high pressures," Phys. Rev. B **96**, 144108 (2017).
[48]S. Qian, X. Sheng, X. Yan, Y. Chen, and B. Song, "Theoretical study of stability and superconductivity of ScH_n ($n = 4 - 8$) at high pressure," Phys. Rev. B **96**, 094513 (2017).
[49]K. Abe, "High-pressure properties of dense metallic zirconium hydrides studied by *ab initio* calculations," Phys. Rev. B **98**, 134103 (2018).
[50]S. Yi, C. Wang, H. Jeon, and J.-H. Cho, "Stability and bonding nature of clathrate H cages in a near-room-temperature superconductor LaH_{10}," Phys. Rev. Mater. **5**, 024801 (2021).
[51]A. Kokalj, "XCrySDen—a new program for displaying crystalline structures and electron densities," J. Mol. Graphics Modell. **17**, 176–179 (1999).
[52]J. Bi, Y. Nakamoto, P. Zhang, Y. Wang, L. Ma, Y. Wang, B. Zou, K. Shimizu, H. Liu, M. Zhou, H. Wang, G. Liu, and Y. Ma, "Stabilization of superconductive La–Y alloy superhydride with T_c above 90 K at megabar pressure," Mater. Today Phys. **28**, 100840 (2022).
[53]D. C. Lonie, J. Hooper, B. Altintas, and E. Zurek, "Metallization of magnesium polyhydrides under pressure," Phys. Rev. B **87**, 054107 (2013).
[54]Y.-L. Hai, N. Lu, H.-L. Tian, M.-J. Jiang, W. Yang, W.-J. Li, X.-W. Yan, C. Zhang, X.-J. Chen, and G.-H. Zhong, "Cage structure and near room-temperature superconductivity in TbH_n (n = 1–12)," J. Phys. Chem. C **125**, 3640–3649 (2021).